Journal of Biomedical Optics

BiomedicalOptics.SPIEDigitalLibrary.org

Rapid and high-resolution imaging of human liver specimens by full-field optical coherence tomography

Yue Zhu
Wanrong Gao
Yuan Zhou
Yingcheng Guo
Feng Guo
Yong He

SPIE.

Rapid and high-resolution imaging of human liver specimens by full-field optical coherence tomography

Yue Zhu,[a] Wanrong Gao,[a,*] Yuan Zhou,[b] Yingcheng Guo,[a] Feng Guo,[c] and Yong He[a]
[a]Nanjing University of Science and Technology, Department of Optical Engineering, 200 Xiao Ling Wei, Nanjing, Jiangsu 210094, China
[b]Nanjing University, Medical School of Nanjing University, 22 Hankou, Nanjing, Jiangsu 210093, China
[c]Xi'an Railway Vocational & Technical Institute, Department of Mechanical and Electronic Engineering, 133 Zi Qiang Xi Lu, Xian, Shaanxi 710014, China

Abstract. We report rapid and high-resolution tomographic *en face* imaging of human liver specimens by full-field optical coherence tomography (FF-OCT). First, the arrangement of the FF-OCT system was described and the performance of the system was measured. The measured axial and lateral resolutions of the system are 0.8 and 0.9 μm, respectively. The system has a sensitivity of ~60 dB and can achieve an imaging rate of 7 fps and a penetration depth of ~80 μm. The histological structures of normal liver can be seen clearly in the *en face* tomographic images, including central veins, cords of hepatocytes separated by sinusoidal spaces, and portal area (portal vein, the hepatic arteriole, and the bile duct). A wide variety of histological subtypes of hepatocellular carcinoma was observed in *en face* tomographic images, revealing notable cancerous features, including the nuclear atypia (enlarged convoluted nuclei), the polygonal tumor cells with obvious resemblance to hepatocytes with enlarged nuclei. In addition, thicker fibrous bands, which make the cytoplasmic plump vesicular nuclei indistinct, were also seen in the images. Finally, comparison between the portal vein in a normal specimen versus that seen in the rare type of cholangiocarcinoma was made. The results show that the cholangiocarcinoma presents with a blurred pattern of portal vein in the lateral direction and an aggregated distribution in the axial direction; the surrounding sinusoidal spaces and nuclei of cholangiocarcinoma are absent. The findings in this work may be used as additional signs of liver cancer or cholangiocarcinoma, demonstrating capacity of FF-OCT device for early cancer diagnosis and many other tumor-related studies in biopsy. [DOI: 10.1117/1.JBO.20.11.116010]

Keywords: medical optics; liver tissue; optical coherence tomography; biopsy.

Paper 150435RR received Jul. 2, 2015; accepted for publication Nov. 2, 2015; published online Nov. 30, 2015.

1 Introduction

According to the World Cancer Report 2014 written by the World Health Organization,[1] the mortality rates of liver cancer in China ranked first worldwide. Additionally, hepatocellular carcinoma (HCC) is the most common primary hepatic malignancy of adults, with 20,000 new cases diagnosed in the United States and approximately half a million cases diagnosed worldwide each year; the overall prognosis is poor, with a five-year survival rate <12%.[2]

At present, the procedure for diagnosing liver cancer includes physical exam, blood tests, computed tomography, magnetic resonance imaging, ultrasound test, and biopsy, among which biopsy is the last step and is regarded as the gold standard. However, conventional biopsy has some serious limitations. First, it requires 1 to 3 days to make paraffin sections from biopsy tissue before the surgery, yet the slice processing may influence pathological diagnosis due to rather thin sections (~5 μm). Moreover, while hematoxylin–eosin staining (H-E staining) is capable of helping doctors to identify normal tissue and pathological tissue morphology, it is difficult to tell watery degeneration or glycogen when lipid droplets become the shape of vacuoles after staining. Sometimes, uneven dyeing may result in significant wastage of tissue, which becomes a major concern for small biopsies that could contain the suspicious lesion in its entirety.

Full-field optical coherence tomography (FF-OCT) is an interferometric technique that utilizes spatially incoherent illumination and array detection to provide high-resolution transverse images of reflected light within biological specimens. Light sources with a broad spectrum (typically a halogen source) are used for displaying micron-level axial structures. The lateral resolution is improved by the high objective numerical aperture (NA). FF-OCT enables high resolution over the full field of observation. As we know, biology applications of FF-OCT technology with an isotropic resolution around 1 μm will be useful for clinicians and surgeons. Currently, FF-OCT has been used in studies in developmental biology. Examples include noninvasive three-dimensional (3-D) subcellular live imaging of preimplantation mouse embryos with no need for dye labeling for quantitatively measuring the factors relating to early patterning and polarity in preimplantation embryonic development,[3] fresh unstained human lobectomy sample imaging for identifying, and differentiating lung tumors from non-neoplastic lung tissue,[4] measuring the brain refractive index *in vivo*,[5] identifying cancer cells by measuring the refractive index distribution across a single live cell,[6] generating cross-section of *ex vivo* tissues from different rat organs,[7] obtaining *en face* tomographic images of *in vivo* human lip,[8] nondestructively evaluating

*Address all correspondence to: Wanrong Gao, E-mail: wgao@njust.edu.cn

1083-3668/2015/$25.00 © 2015 SPIE

film coatings applied to spherical pellets,[9] observing the blood vessel in dermis, and tracing the flowing of the red blood cells.[10]

Although FF-OCT has been previously utilized to assess histological features of *ex vivo* tissues, to the best of our knowledge, there is no report about human liver cancer tissue imaging based on FF-OCT. In this paper, we explored the potential usage of FF-OCT for identifying and differentiating liver cancer cells in fresh, *ex vivo* human liver specimens without H-E staining or fluorescein labeling. We first describe the instrument and performance of FF-OCT system. Then the fine structures of human liver with spatial resolution around 1 μm will be presented. Using this FF-OCT system, we also compared nuclei, fibrous bands, and portal veins in normal and abnormal liver tissue, respectively. All these efforts were intended to make rapid and high-resolution diagnosis.

2 Full-Field Optical Coherence Tomography Instrument

The arrangement of the FF-OCT system is presented in Fig. 1. For the purpose of high resolution and speed, we developed a single chip to synchronize charge-coupled device (CCD), piezoelectric stage actuator (PZT) (AE0505D18F, Thorlabs), and two electric displacement platforms combining with the related algorithms. The system is based on the Linnik interference microscope geometry (see Fig. 1) with a 20-W tungsten halogen lamp in an improved Köhler illumination system.[11] The central wavelength and spectral half-width of the tungsten halogen lamp spectra are 550 and 200 nm, respectively. A pair of identical microscope objectives (20×, 0.5 numerical, Olympus) is placed in both arms. The polished surface of a $Y_3Al_5O_{12}$ (YAG) crystal rod is used as a reference mirror and provides an 8% reflectivity reference surface. In our initial experiments, YAG crystal was chosen as a reference mirror. The reflectivity equals 8%. It is, of course, not good for the optimization of system sensitivity. An FF-OCT system coupled with water-immersion (the refractive index of the medium is 1.33) objectives is under construction; thus a reference reflectivity of 2% can be realized, which is much closer to the optimum value for the imaging of most biological tissues.[12] The interference images are digitized by a CCD camera (Matrox Iris GT300, 640 pixel × 480 pixel, pixel size is 7.4 × 7.4 μm) working at a maximum rate of 110 frames per second (fps).

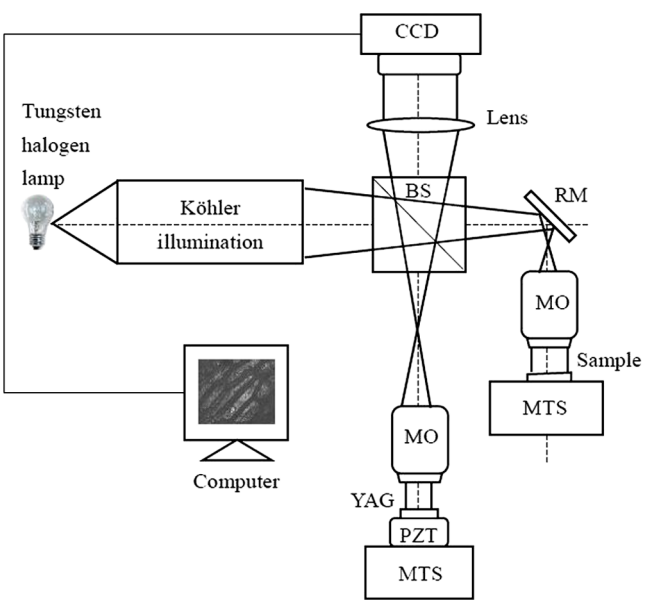

Fig. 1 Schematic representation of the full-field optical coherence tomography (FF-OCT) setup. AS, aperture stop; FS, field stop; BS, beam splitter; MO, microscope objectives; RM, reflective mirror (silver); YAG, $Y_3Al_5O_{12}$ crystal; MTS, motorized translation stage.

The program can be modified at arbitrary rate in appropriate for different samples easily. If the sample is *in vivo*, such as human skin, the acquisition rate should be accelerated to reduce the motion artifacts. While the sample is *ex vivo* tissue, it should be slowed down to normal speed to reduce the motion artifacts due to the broad bandwidth, because the phase shifting is based only on the central wavelength, or it should also make more periods of shifting the PZT in same depth in order to raise the signal-to-noise ratio (SNR). At present, the rate of the program we developed is for PZT range from 20 to 1 Hz while the CCD we used has the maximum rate of 110 fps. The program remains to be upgraded to reach the extreme speed of CCD.

The YAG crystal was attached to a PZT to make it oscillate a sinusoidal phase modulation at the frequency $f = 7/4$ Hz (see Fig. 2). The CCD camera was synchronized with the PZT oscillation and triggered at the frequency $4f = 7$ Hz to capture four images per modulation period. N periods of four images could be accumulated to increase the SNR, as it can cover more abundant structures. Moreover, a motorized axial translation was used to get 3-D information of tissues with dynamic coherent focus technique for the intention of deeper imaging depth.[13,14] The sample arm can be scanned by moving the motorized translation stage for the purpose of depth information. The finest distance is 0.1 μm, which is much smaller than axial resolution. Eventually, the signal will be extracted from the interference fringe intensity, corresponding to the light that is backscattered from a particular slice inside the sample.

With broad-spectrum illumination, interference occurs only when the optical path lengths of two interferometer arms are nearly equal. The interference signal contrast varies according to a coherence function that drops off rapidly when the optical path-length difference exceeds the coherence of the illumination source. The coherence length is inversely proportional to the spectrum width of the illumination source. Thus, the image formed on the CCD detector array consists of the interference

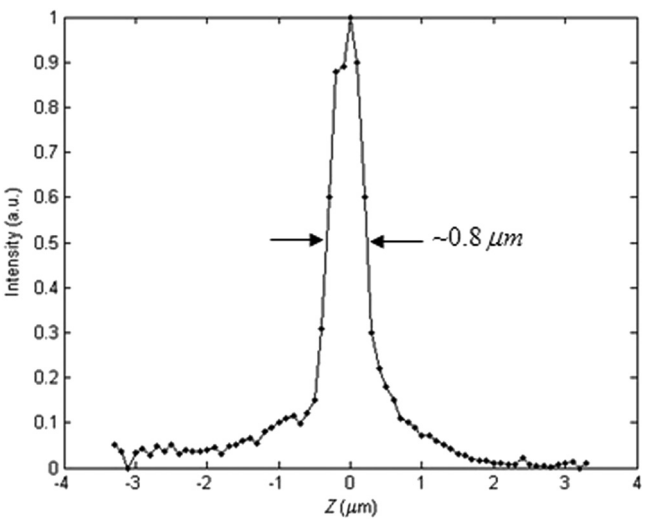

Fig. 2 The reflected light intensity of different positions.

of the image of the sample with the uniform image of the reference mirror, upon which is superimposed the incoherent light from reflections and backscatterings from different depths in the sample and from unwanted reflections in the microscope itself. Without phase modulation and two arms in coherence, the intensity I at any pixel (x, y) of the CCD array can be expressed as[15]

$$I(x,y,t) = \bar{I}(x,y) + A(x,y)\cos[\phi(x,y) + \Psi \sin(2\pi f t + \theta)], \tag{1}$$

where $\bar{I}(x,y)$ is the average intensity, $\phi(x,y)$ denotes the optical phase, $\Psi \sin(2\pi f t + \theta)$ represents the sinusoidal phase modulated by PZT controller, and $A(x,y)$ denotes the intensity of the coherent signal, proportional to the time-averaged cross correlation of the sample and reference optical fields. According to the algorithm, an *en face* OCT image can be obtained from the following equation:[12]

$$\begin{aligned} A(x,y) = \{&[I(x,y,1) - I(x,y,2) - I(x,y,3) + I(x,y,4)]^2 \\ &+ [I(x,y,1) - I(x,y,2) + I(x,y,3) - I(x,y,4)]^2\}^{1/2}. \end{aligned} \tag{2}$$

By means of synchronizing CCD and PZT, the CCD recorded four pictures in each time and the pictures contained the interference information. The proposed algorithm averaged a large amount [$N = 10$, in Eq. (3)] of *en face* images to improve the image contrast. For instance, it takes 450 s to generate a 3-D data stack, the 3-D size of which is $385 \times 288 \times 80\ \mu m^3$. Thus, the tomographic image A^* is calculated with the following formula:

$$\begin{aligned} A^*(x,y) = \frac{1}{N}\sum_{i=1}^{N} \{&[I_i(x,y,1) - I_i(x,y,2) - I_i(x,y,3) + I_i(x,y,4)]^2 \\ &+ [I_i(x,y,1) - I_i(x,y,2) + I_i(x,y,3) - I_i(x,y,4)]^2\}^{1/2}. \end{aligned} \tag{3}$$

Dispersion mismatch occurs when light rays propagate inside the tissue. When focused into tissues, the focus is shifted forward while the coherence plane goes backward, thus leading to interference signal decrease and defocus signal increase. As a result, the optimum spot should be found by moving the reference arm to match the position of the focal plane and of the plane of zero path difference.[16] We used this way to optimize the measurement for different depth.

3 Performance

3.1 *Axial Resolution*

Within a Gaussian line shape for the light source, the axial resolution is generally half of the coherence length, but for an ultra-wide-bandwidth light source, the following formula for the axial resolution d_z should be used:[14,17,18]

$$d_z = \frac{1.78\pi}{\Delta\kappa_z(1 + \cos\theta_0)}, \tag{4}$$

$$\begin{aligned} \Delta\kappa_z &= 2\kappa_0(1 - \cos\theta_0) + 2\Delta\kappa' \\ &= 2\kappa_0(1 - \cos\theta_0) + \Delta\kappa(1 + \cos\theta_0). \end{aligned} \tag{5}$$

Here, $\kappa_0 = \lambda_0/2\pi$ represents wavenumber, λ_0 is the center wavelength, θ_0 represents incidence angle, and $\Delta\kappa$ denotes the bandwidth. In air ($n = 1$), with NA = 0.5 and a wavelength $\lambda_0 =$ 550 nm, the theoretical resolution is 0.5 μm.

We then measured the axial resolution of the system by placing a reflective mirror as a sample in the sample arm and moving the YAG crystal in the reference arm with a step of 0.1 μm with the motorized translation stage. The *en face* tomographic images of different axial positions were then reconstructed. Finally, the point spread function (PSF) along the axial direction was acquired (see Fig. 2). The full width at half maximum (FWHM) of the PSF is a measure of the axial resolution, ~0.8 μm. The difference between the measured value and the theoretical one (0.5 μm) is mainly due to optical aberration. Beside the optical aberration, dispersion mismatch may also be a big issue. However, only upper surface is detected during measuring. Therefore, the dispersion mismatch is mainly due to the optical system. Note that an extra mirror was used in the sample arm to locate the biological tissue. In addition, the different properties of reflective mirror (BK9) in the sample arm and the YAG crystal in the reference arm are another source, which would definitely affect the conjugate relationship in system. Apart from these, the optical aberration caused by beam splitter (BS) and microscope objectives also influenced the axial resolution.

3.2 *Lateral Resolution*

The lateral resolution of an imaging system is commonly defined as the FWHM of the PSF in lateral direction. In a conventional diffraction-limited optical system, PSF can be expressed as the well-known Airy function, which depends on optical wavelength and the NA, so the lateral resolution d_x is

$$d_x = \frac{0.61\lambda_0}{\mathrm{NA}}. \tag{6}$$

In air ($n = 1$), with NA = 0.5 and a wavelength $\lambda_0 = 550$ nm, the theoretical resolution is $d_z = 0.7$ μm.

We used a 1951 USAF resolution test chart as a sample to measure lateral resolution by recording an intensity profile across three lines of group 6. The edge response is the convolution of a perfect edge with the PSF and the reflection intensity changes with the lateral location. In Fig. 3, the USAF resolution test chart was imaged and the edge response (blue line) with NA = 0.5 was displayed. The 20 to 80% (two dotted lines in Fig. 3) width of the intensity profile was measured to be 0.9 μm, slightly larger than the theoretical prediction of 0.7 μm mainly because of the optical aberrations.

3.3 *Sensitivity*

We measured the sensitivity of our system by inserting a neutral-density filter (NDF) into the reference arm to create a reference mirror with −26 dB reflectivity (equivalent to $R_{\mathrm{ref}} = 2\%$). The optical power of the beam from the reference arm was adjusted with the NDF until it saturated the pixel depth of the CCD camera. On the other hand, the top surface of a clean glass plate (GP), of which the reflectivity is 4% (−23.9 dB), was used as a sample for evaluating the sensitivity. GP was moved

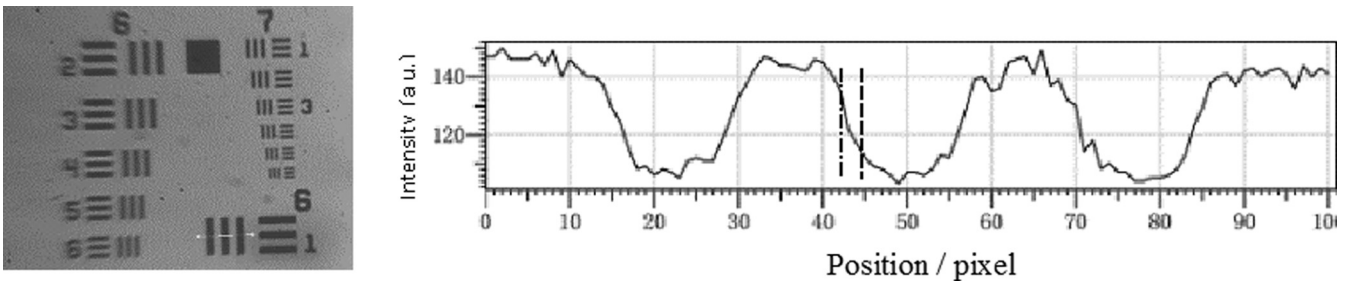

Fig. 3 The edge response of 1951 USAF resolution test chart.

along the axial direction with each step of 0.1 μm by controlling the precise motorized translation stage with 10 accumulations, in one pixel located at the center of the image, and a mass of the *en face* tomographic images was acquired at the depths of ~60 μm. A background noise of ~ -80 dB was measured and finally the measured sensitivity was almost ~60 dB.

4 Sample Preparation

After the surgery, the tissue was immersed in formalin liquid immediately and then taken to our lab. On the next stage, the samples to be imaged were cut in cross-section (2 to 5 mm thick) and immersed in an isotonic solution of phosphate-buffered saline.

5 Results

Figure 4 shows the *en face* tomographic images of normal *ex vivo* human liver tissues obtained with our FF-OCT system. Normal liver architectures are mainly composed of cords of hepatocytes radiating from central veins [Fig. 4(a)] and extending to the portal areas [Figs. 4(d) and 4(e)]; these cords are separated by sinusoidal spaces [Figs. 4(b) and 4(c)].[7,19–26] Two *en face* tomographic images in different depths of unstained fresh liver tissue showed detailed components of basic liver lobules, with portal area [Figs. 4(d) and 4(e)], including branch of portal vein, branch of hepatic artery, and a small bile ductule. Apart from these, some liver cells can be distinguished as white arrowhead pointed in Figs. 4(d) and 4(e) of different depths.

Figure 5 depicts the *en face* tomographic images of the cancerous liver tissue by FF-OCT system, demonstrating the presence of the nuclear atypia of HCC in the differentiation of the hepatic parenchyma cells; these cells with large round nuclei were deemed to be hepatocytes.[23] It can be seen from Fig. 5(a) that the cytoplasm is surrounded by a round nuclei of HCC [white arrows in Fig. 5(a)], the size of which is 20 μm. Moreover, in Fig. 5(b), the hepatocytes [arrowhead in Fig. 5(b)] are separated by sinusoidal spaces, central veins. On comparison, the nuclear atypia of the cancerous one is with the form of enlarged convoluted nuclei (35 μm) but retaining the cytoplasmic quality of normal hepatocytes.

The *en face* tomographic images in Fig. 6 show the differences in fibrous bands between normal and cancerous tissues. On comparison of Fig. 6(a) with Fig. 6(b), the fibrous bands in tumor tissue are characterized by a solid growth pattern with large tumor nodules separated by thick fibrous bands [two

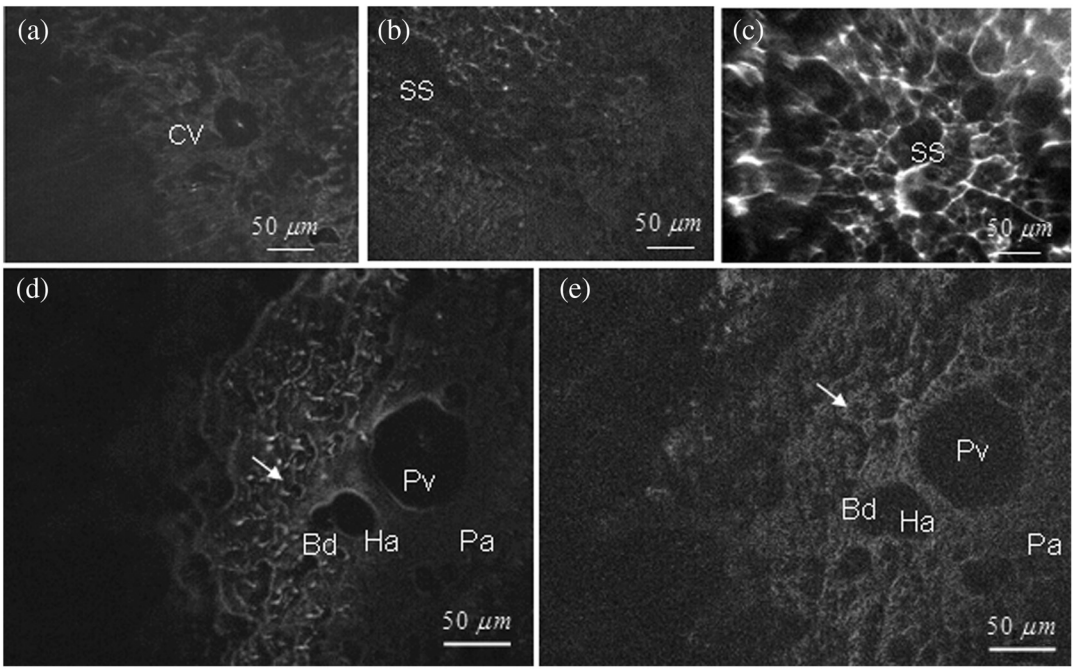

Fig. 4 *En face* FF-OCT images of normal liver tissue: (a) central vein, (b) and (c) cords separated by sinusoidal spaces, (d) portal area at the depth of 35 μm, and (e) portal area at the depth of 45 μm. CV, central veins; SS, sinusoidal spaces; Pa, portal area; Ha, hepatic artery; Bd, bile ductule.

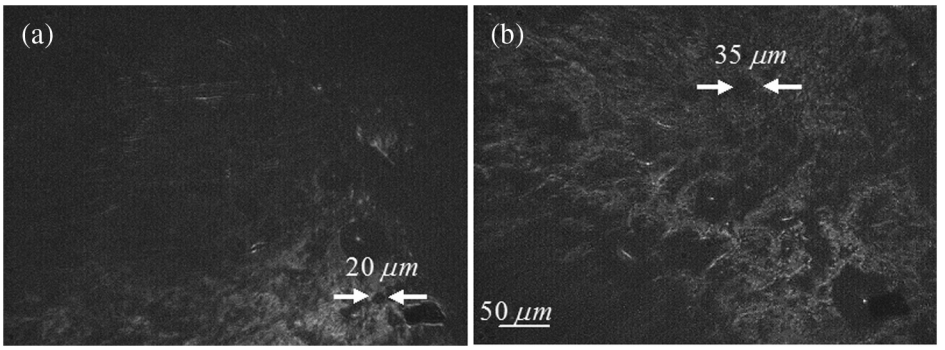

Fig. 5 *En face* FF-OCT images of liver tissue: (a) normal tissue and (b) cancerous tissue.

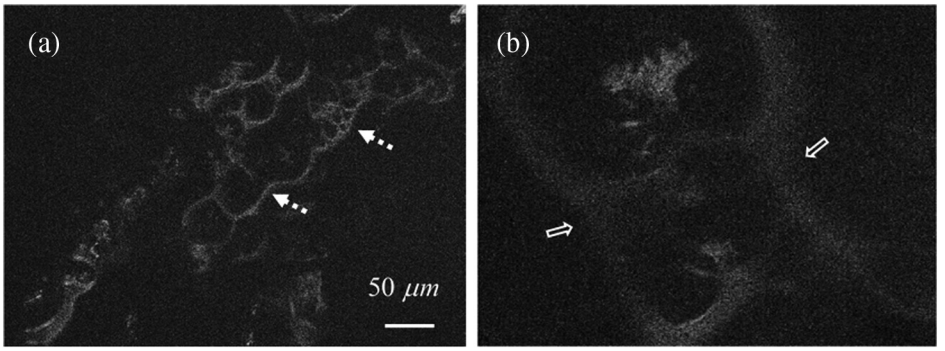

Fig. 6 *En face* FF-OCT images of liver tissue: (a) fibrous bands in normal tissue (two dotted arrows) and (b) thicker fibrous bands in cancerous tissue (two white arrowheads).

white arrowheads in Fig. 6(b)]. The malignant nature of HCC in low differentiation degree is obvious by the very abnormal architecture because thicker fibrous band is one of the features for liver cancer.[27]

Cholangiocarcinoma (bile duct cancer) is rarely reported due to the lower probability of disease incidence. We also imaged the intensity *en face* tomographic images of portal vein, which revealed the distinction of cholangiocarcinoma within the differentiation of epithelial cells, in Fig. 7. The normal portal vein is shown in Fig. 7(a); we can see the clear structure of portal vein from the graph and the blurred pattern of the same region in the center of the image in Fig. 7(b). In addition, the blurred portal vein is surrounded by a rather small number of sinusoidal spaces combined with nuclei but not quite near the center area, in Fig. 7(c).

The cross-sectioned images (B-scan) can also be generated by our FF-OCT system. By moving the sample step by step in the axial direction, it can acquire a stack of tomographic images. Once a 3-D data set is recorded, sections of arbitrary geometries can be extracted. Figure 8 shows the *en face* tomographic images of the liver tissue. Each image corresponds to a field of $385 \times 288 \times 80\ \mu m^3$. The 3-D FF-OCT images of normal portal vein [in Fig. 8(a)] are compared with the cancerous one [in Fig. 8(b)]. The cross lines displayed in Figs. 8(a) and 8(b) represent corresponding sections' positions.

As revealed by Figs. 7 and 8, a more uniform distribution exists in normal tissue, as can be seen from the image in Fig. 8(a), which displays two evenly distributed layers in *X*-*Z*, *Y*-*Z* directions and each layer has the same length; however, the cancerous tissue of Fig. 8(b) in axial section is gathering to central part and with different lengths, while in the lateral section, the pattern of the cancerous one [see Fig. 8(b), *X*-*Y*] is more blurred and shows polymerization in the center of portal vein. It is shown that the sinusoidal spaces and the nuclei in liver tissue are broken and exist far away from the portal area.

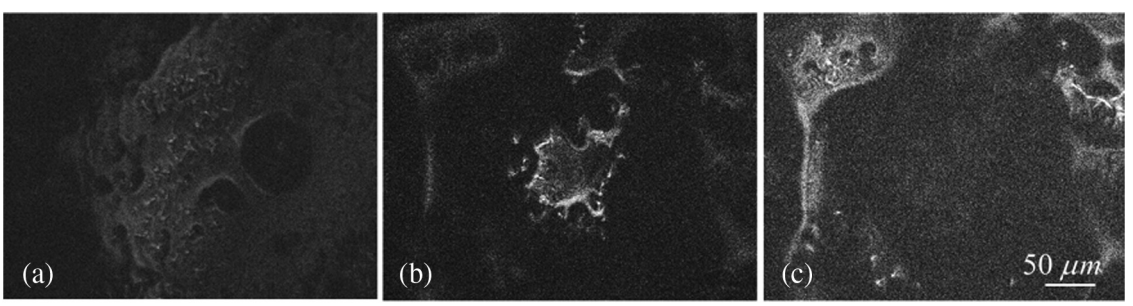

Fig. 7 *En face* FF-OCT images of portal veins of normal and bile duct cancer: (a) normal portal vein, (b) portal vein at the depth of 26 μm below the surface, and (c) portal area at the depth of 42 μm.

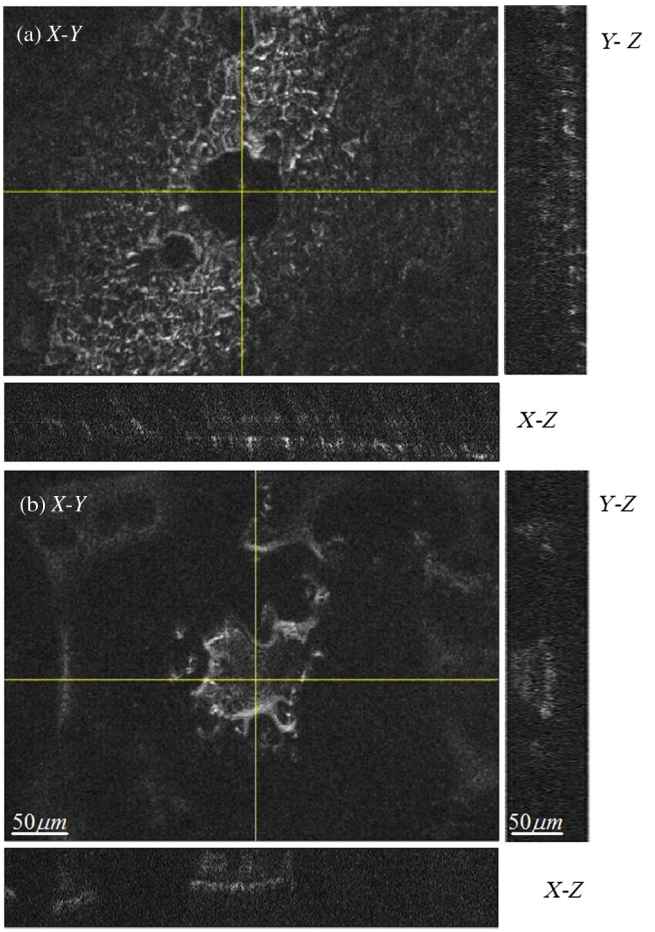

Fig. 8 Three-dimensional (3-D) images of portal vein with a depth interval of 1 μm. Each image consists of 640 pixels × 480 pixels and 3-D data are $385 \times 288 \times 80$ μm^3: (a) normal portal veins FF-OCT images with *X-Y*, *Y-Z*, and *X-Z* directions and (b) portal vein of bile duct cancer FF-OCT images with *X-Y*, *Y-Z*, and *X-Z* directions.

6 Discussion

Wide-field imaging capability can help to find the region of interest of the sample based on light reflection. High lateral resolution was obtained by using a pair of relatively high-NA (0.5) microscope objectives and the high axial resolution due to the broad bandwidth (~200 μm). In FF-OCT system, two arms of interference were identical so that the object plane and image plane formed a conjugate relationship; in this case, the dispersion during the optical paths need not to be taken into account. Moreover, it is a time-saving and noninvasive method, simplifying the preparation for the specimens, such as frozen-section or paraffin-section. Compared with other international FF-OCT research groups, some of them made efforts in calculating the distributions of refraction of sidle rat kidney cell to distinguish the normal from cancer tissue, but it remained needing a considerable number of refraction indices (index) to trade off whether it is cancerous. At the same time, it was an indirect way to show the details. The purpose of the research reported in this paper was to demonstrate an ability to identify, assess the microstructure of normal and cancer liver tissue, and help clinical diagnosis, judging the types and stages of liver cancer accurately.

7 Conclusion

In this article, a full-field optical coherence tomography for tissue imaging system was developed and applied to image human liver *ex vivo* noninvasively. The sinusoidal spaces of superficial region of liver, center vein, and portal area, including information of branch of portal vein, branch of hepatic artery, and a small bile ductile can be seen clearly in the *en face* tomographic images. In addition, the nuclear atypia and thicker fibrous bands of HCC can be observed in *en face* tomographic image. It is also found that, compared with normal portal area, the different structures and distribution characteristics in lateral and axial direction of cholangiocarcinoma were also presented in its *en face* tomographic images.

Acknowledgments

This research was supported by the National Natural Science Foundation of China (61275198, 60978069, and 11473017). The study was approved by the Ethics Committee of Wuxi No. 3 People's Hospital.

References

1. R. Siegel et al., "Cancer statistics, 2014," *CA: Cancer J. Clin.* **64**(1), 9–29 (2014).
2. E. Quist et al., "Medullary-like hepatocellular carcinoma: an unusual histologic variant," *Am. J. Clin. Pathol.* **142**(5), 670–674 (2014).
3. Z. Zhi, Y. Jung, and R. K. Wang, "Label-free 3D imaging of microstructure, blood, and lymphatic vessels within tissue beds in vivo," *Opt. Lett.* **37**(5), 812–814 (2012).
4. M. Jain et al., "Full-field optical coherence tomography for the analysis of fresh unstained human lobectomy specimens," *J. Pathol. Inf.* **4**, 26 (2013).
5. J. Binding et al., "Brain refractive index measured in vivo with high-NA defocus-corrected full-field OCT and consequences for two-photon microscopy," *Opt. Express* **19**(6), 4833–4847 (2011).
6. W. J. Choi et al., "Full-field optical coherence microscopy for identifying live cancer cells by quantitative measurement of refractive index distribution," *Opt. Express* **18**(22), 23285–23295 (2010).
7. M. Jain et al., "Modified full-field optical coherence tomography: a novel tool for rapid histology of tissues," *J. Pathol. Inf.* **2**(28), 82053 (2011).
8. A. Latrive and A. C. Boccara, "In vivo and in situ cellular imaging full-field optical coherence tomography with a rigid endoscopic probe," *Biomed. Opt. Express* **2**(10), 2897–2904 (2011).
9. C. Li et al., "Non-destructive evaluation of polymer coating structures on pharmaceutical pellets using full-field optical coherence tomography," *J. Pharm. Sci.* **103**(1), 161–166 (2014).
10. C. C. Tsai et al., "Full-depth epidermis tomography using a Mirau-based full-field optical coherence tomography," *Biomed. Opt. Express* **5**(9), 3001–3010 (2014).
11. X. Zhu, W. Gao, and Y. Zhu, "Improved Kohler illumination-based full-field optical coherence tomography system," *Acta Opt. Sin.* **34**(5), 0511002 (2013) (In Chinese).
12. A. Dubois et al., "Ultrahigh-resolution full-field optical coherence tomography," *Appl. Opt.* **43**(14), 2874–2883 (2004).
13. J. M. Schmitt, S. L. Lee, and K. M. Yung, "An optical coherence microscope with enhanced resolving power in thick tissue," *Opt. Commun.* **142**(4–6), 203–207 (1997).
14. F. Lexer et al., "Dynamic coherent focus OCT with depth-independent transversal resolution," *J. Mod. Opt.* **46**(3), 541–553 (1999).
15. A. Dubois et al., "High-resolution full-field optical coherence tomography with a Linnik microscope," *Appl. Opt.* **41**(4), 805–812 (2002).
16. S. Labiau et al., "Defocus test and defocus correction in full-field optical coherence tomography," *Opt. Lett.* **34**(10), 1576–1578 (2009).
17. G. S. Kino and S. S. Chim, "Mirau correlation microscope," *Appl. Opt.* **29**(26), 3775–3783 (1990).

18. Y. Zhu and W. Gao, "High-resolution full-field optical coherence tomography for biological tissue," *Chin. J. Lasers* **41**(8), 0804002 (2014) (In Chinese).
19. A. K. Christensen, "Frozen thin sections of fresh tissue for electron microscopy, with a description of pancreas and liver," *J. Cell Biol.* **51**(3), 772–804 (1971).
20. T. Kanai et al., "Pathology of small hepatocellular carcinoma. A proposal for a new gross classification," *Cancer* **60**(4), 810–819 (1987).
21. E. Kay et al., "Mild abnormalities in liver histology associated with chronic hepatitis: distinction from normal liver histology," *J. Clin. Pathol.* **50**(11), 929–931 (1997).
22. J. Lechago, "Frozen section examination of liver, gallbladder, and pancreas," *Arch. Pathol. Lab. Med.* **129**(12), 1610–1619 (2005).
23. J. Baratta et al., "Cellular organization of normal mouse liver: a histological, quantitative immunocytochemical, and fine structural analysis," *Histochem. Cell Biol.* **131**(6), 713–726 (2009).
24. E. Quist, G. Talmon, and C. Hartman, "Medullary-like hepatocellular carcinoma: an unusual histologic variant," *Am. J. Clin. Pathol.* **142**(5), 670 (2014).
25. S. S. Arsad, N. M. Esa, and H. Hamzah, "Histopathologic changes in liver and kidney tissues from male Sprague Dawley rats treated with Rhaphidophora Decursiva (Roxb.) Schott extract," *J. Cytol. Histol. S* **4**, 001-006 (2014).
26. J. Misdraji, "Embryology, anatomy, histology, and developmental anomalies of the liver," in *Sleisenger and Fordtran's Gastrointestinal and Liver Disease*, M. Feldman, L. S. Friedman, and L. J. Brandt, Eds., pp. 1203-1204, W. B. Saunders, Philadelphia (2010).
27. S. Ali and V. Shah, "Small-duct primary sclerosing cholangitis with hepatocellular carcinoma requiring liver transplantation," *Hepatobiliary Pancreat. Dis. Int.* **9**(2), 208–212 (2010).

Yue Zhu received her BS degree in optics engineering from Nanjing University of Science and Technology in 2012 and then continued studying for a PhD in optics engineering in Nanjing University of Science and Technology. Her research topic is full-field optical coherence tomography.

Wanrong Gao received his PhD from Xi'an Institute of Optics and Fine Mechanics, Chinese Academy of Sciences in 1996. He worked as a postdoctoral fellow at Nanjing University of Science and Technology from October 1996 to October 1998. He worked at Professor So's lab at Massachusetts Institute of Technology from February 2002 to February 2003 and Professor Izatt's lab at Duke University from March 2011 to March 2012 as a visiting scientist. Now he is a professor in the Department of Optical Engineering, Nanjing University of Science and Technology. He conducts research in biomedical optics and spectroscopy.

Yuan Zhou received his BS degree in clinical medicine combined with Chinese traditional medicine and Western medicine from Nanjing University of Chinese Medicine in 2012 and then continued studying for his MS in clinical medicine in Nanjing University. His research topic is liver cancer.

YingCheng Guo received his BS degree in optics engineering from Nanjing University of Science and Technology in 2014 and then continued studying for his MS degree in physical electronics at Nanjing University of Science and Technology. His research topic is full field-optical coherence tomography.

Feng Guo received his BS in physics from Shanxi Normal University in 2002. Currently, he is working as a lecturer in the Department of Mechanical and Electronic Engineering, Xi'an Railway Vocational and Technical Institute. His current interest is in the fields of signal processing and system control.

Yong He received his PhD from Nanjing University of Science and Technology in 2004. Currently, he is working as a professor in the Department of Optical Engineering, Nanjing University of Science and Technology. He conducts research in the area of optical interference metrology.